Magnetostructural coupling and magnetodielectric effects in the *A*-site cation-ordered spinel $LiFeCr_4O_8$

Rana Saha,[1] R. Dhanya,[1] Christophe Bellin,[2] Keevin Béneut,[2] Arpan Bhattacharyya,[3] A. Shukla,[2] Chandrabhas Narayana,[1] E. Suard,[4] J. Rodríguez-Carvajal,[4] and A. Sundaresan[1]

[1]*Chemistry and Physics of Materials Unit and International Centre for Materials Science, Jawaharlal Nehru Centre for Advanced Scientific Research, Jakkur P.O., Bangalore 560 064, India*

[2]*Sorbonne Universités, UPMC Université Paris 6, UMR 7590, IMPMC, F-75005 Paris, France*

[3]*Saha Institute of Nuclear Physics, Bidhannagar, Kolkata 700064, India*

[4]*Institut Laue Langevin, 71 avenue des Martyrs, 38042 Grenoble, France*

(Received 22 September 2017; revised manuscript received 10 November 2017; published 27 December 2017; corrected 9 January 2018)

The *A*-site cation-ordered spinel $LiFeCr_4O_8$ is a unique system which manifests properties of the frustrated pyrochlore lattice, including the breathing distortion and antiferromagnetic coupling between *A* and *B* sites. This compound crystallizes in a cubic spinel structure with a noncentrosymmetric space group ($F\bar{4}3m$), where Li^{+} and Fe^{3+} ions are ordered in a zinc-blende-type manner at the *A* site and Cr^{3+} ions at the *B* site form a breathing pyrochlore lattice. It undergoes a ferrimagnetic transition at $T_N \sim 94$ K, below which temperature-dependent magnetization data exhibit a maximum at $T_{SG} \sim 60$ K, corresponding to a spin-gap arising from breathing distortion. At low temperature ($T_{MS} \sim 23$ K), concurrent structural ($I\bar{4}m2$) and magnetic phase transitions occur because of significant geometrical frustration of the pyrochlore lattice, giving rise to a complex conical magnetic order. Intriguingly, the observed dielectric anomalies at all three magnetic transition temperatures in zero applied magnetic field indicate the occurrence of magnetodielectric effects. Further, the temperature dependence of Raman modes shows three distinct anomalous behaviors that correlate with the dielectric anomalies at T_N, T_{SG}, and T_{MS}, which suggest the presence of spin-lattice coupling.

DOI: 10.1103/PhysRevB.96.214439

I. INTRODUCTION

Magnetic oxides of the general formula AB_2O_4 crystallizing in the spinel structure provide a rich playground to study the magnetic frustration and associated effect on magnetostructural coupling and related physical properties [1–3]. The diverse magnetic properties of the spinel compound arise due to its complex structure, with two different crystallographic sites (*A* and *B*) of different coordination, and strong coupling between spin, lattice, and orbital degrees of freedom [4,5]. Most of the spinel compounds without orbital degeneracy either in the *A* or *B* site crystallize in a cubic structure with the space group $Fd\bar{3}m$. If both the *A* and *B* sites are occupied by magnetic ions, the strong *A*-*B* interaction results in ferrimagnetic ordering at high temperatures, as observed in Fe_3O_4 [6,7]. On the other hand, when the magnetic ions occupy only the *A* site, as in MnX_2O_4 (X = Al, Ga), Co_3O_4, and MAl_2O_4 (M = Fe, Co, Ni), they exhibit various magnetic ground states ranging from a collinear antiferromagnetic state to a spiral spin-liquid state, depending on the ratio of next-nearest-neighbor to nearest-neighbor magnetic interactions [8–12]. In contrast, *B*-site magnetic spinel compounds, e.g., ACr_2O_4 (A = Zn, Cd, Hg), are highly frustrated because they form a pyrochlore network [13–15]. In spite of the fact that both *A*- and *B*-site magnetic spinel compounds crystallize in the cubic structure with the space group $Fd\bar{3}m$, they differ in their magnetostructural ground state [16]. The *A*-site magnetic spinels, with relatively small frustration, do not undergo structural transition at low temperatures. On the other hand, a strong magnetic frustration in the pyrochlore lattice of the *B*-site magnetic spinels drives a structural transition, which is accompanied by a long-range magnetic ordering, through a spin Jahn-Teller effect [17–19] where structural distortion reduces the magnetic frustration which results in the development of long-range antiferromagnetic ordering at low temperatures [20,21]. However, if a Jahn-Teller ion is present in either the *A* or *B* site, the symmetry may be reduced below $Fd\bar{3}m$ and the system can undergo further structural transition at low temperature, as observed in $FeCr_2O_4$ [16].

Recently, a linear magnetoelectric effect was reported in a family of *A*-site magnetic spinels such as $MnGa_2O_4$, $MnAl_2O_4$, Co_3O_4, and $CoAl_2O_4$, exhibiting collinear magnetic ordering [22–24]. The origin of the magnetoelectric effect has been attributed to spin-dependent macroscopic electric polarization as a result of spin-orbit coupling, which modifies the local electric dipole moment associated with the local polar noncentrosymmetric surrounding of oxygen ions [25,26]. The concept of local noncentrosymmetry was extended to a *B*-site magnetic spinel, for example, $ZnCr_2O_4$, where the presence of inversion symmetry at the Cr site is broken by replacing Zn^{2+} with nonmagnetic ions, Li^{+} and Ga^{3+} (In^{3+}), which results in an ordered arrangement at the *A*-site ions and breathing pyrochlore lattice at the Cr site, as reported for $LiMCr_4O_8$ (M = Ga and In) where the symmetry is reduced from $Fd\bar{3}m$ to $F\bar{4}3m$ by losing the inversion center at the Cr site [26]. However, no magnetoelectric effect was observed in these compounds [27]. On the other hand, the In compound is reported to exhibit a spin-gap behavior due to modulation of the Cr-Cr bond distances, which is associated with a sharp dielectric anomaly indicating a spin-lattice coupling [27,28].

In this work, we have replaced the nonmagnetic Ga/In ions in $LiMCr_4O_8$ by Fe^{3+} ions so that one can have magnetic interactions between Fe and Cr ions while retaining the breathing pyrochlore distortion, which may lead to

interesting magnetoelectric properties. Except for an infrared study [29,30], detailed structural information and physical properties are not known for $LiFeCr_4O_8$. Here, we confirm that the compound exhibits a breathing pyrochlore lattice due to ordering of Li^+ and Fe^{3+} ions at the A site. Unlike the corresponding Ga and In compounds, the Fe compound orders magnetically at a higher temperature ($T_N \sim 94$ K) because of antiferromagnetic coupling between the Fe and Cr ions. Upon cooling below the ferrimagnetic transition at 94 K, it undergoes two successive magnetic transitions at low temperatures. The lowest-temperature magnetic transition at 23 K is accompanied by a complete structural phase transition (T_{MS}) to a tetragonal symmetry with the space group $I\bar{4}m2$ to relieve the magnetic frustration among the Cr ions in the pyrochlore lattice. The magnetic anomaly at $T_{SG} \sim 60$ K is believed to be associated with spin-gap, which causes a sharp change in dielectric anomaly. Dielectric anomalies are also observed at the ferrimagnetic transition ($T_N \sim 94$ K) and the magnetostructural transition ($T_{MS} \sim 23$ K), indicating the occurrence of magnetodielectric effects. The magnetodielectric effects are discussed based on spin-lattice coupling as evidenced from the temperature-dependent Raman modes.

II. EXPERIMENT

A polycrystalline sample of $LiFeCr_4O_8$ was synthesized by mixing stoichiometric amounts of Li_2CO_3 (Aldrich Chemical Company, Inc., 99%+), Fe_2O_3 (Alfa Aesar, 99.99%), and Cr_2O_3 (Sigma Aldrich, 99.9%) and heating the mixture in air at 1000 °C for 15 h with a cooling rate of 1 °C/ min with intermittent grinding. The variable-temperature synchrotron x-ray diffraction data were collected in the angular range of 10−80° using x-rays of wavelength 0.91 Å at the Indian Beamline (BL-18B) of Photon Factory, KEK, Japan. A temperature-dependent neutron-diffraction experiment was carried out on the D2B high-resolution powder diffractometer at the Institut Laue-Langevin (ILL) using wavelengths of 1.59 and 2.4 Å. To perform the neutron diffraction, a ∼2.5 g sample was packed in a vanadium can of diameter 6.2 mm. The diffraction data were analyzed using the programs of the FULLPROF Suite [31]. Magnetic measurements were carried out with a vibrating sample magnetometer in a Superconducting Quantum Interference Device Magnetometer (SQUID, MPMS3, Quantum Design, USA) in the temperature range of 2–390 K. The temperature-dependent specific heat (C_p) was measured in a Physical Property Measurement System (PPMS, Quantum Design, USA). To prepare a capacitor, conducting silver paint was applied on both sides of the pellet and dried under an infrared lamp. The capacitor was mounted on a multifunction probe that was inserted into the PPMS, which allowed access to the temperature and the magnetic field. The temperature- and magnetic-field-dependent capacitance was measured using an LCR (Agilent E4980A) meter by applying a small ac bias of 500 mV. Raman spectroscopy was carried out using a 514.5 nm Argon laser with a power of ∼0.7 mW at the sample. The scattered light was analyzed using a triple spectrometer (Jobin-Yvon, T64000) equipped with a confocal microscope in combination with a liquid-nitrogen-cooled multichannel charge-coupled device detector. For the temperature-dependent studies, the sample was mounted in vacuum on a cold finger of a custom-built helium flow cryostat.

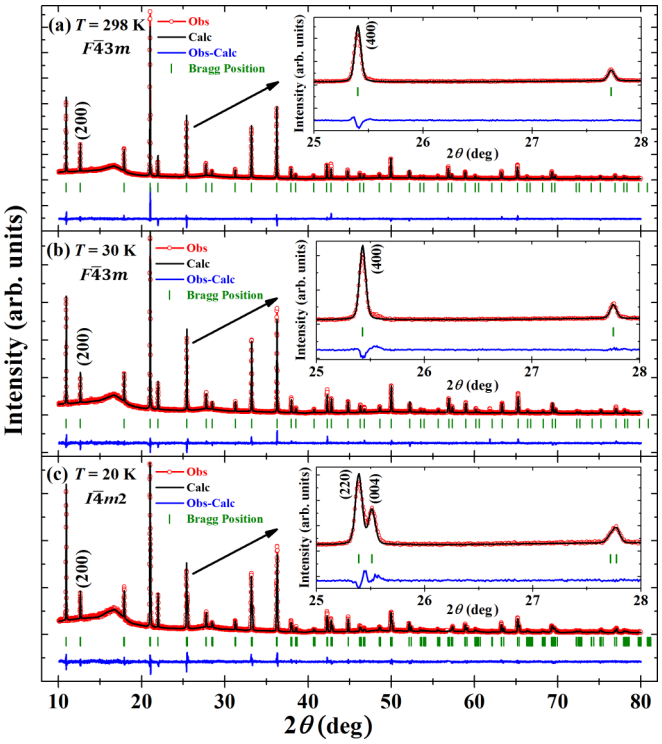

FIG. 1. Rietveld refinements on the synchrotron x-ray diffraction data of $LiFeCr_4O_8$ collected at (a) 298 K, (b) 30 K, and (c) 20 K with $\lambda = 0.91$ Å. Insets of (a)–(c) show the lowering of symmetry from (a),(b) $F\bar{4}3m$ to (c) $I\bar{4}m2$ upon cooling below the magnetostructural transition ($T_{MS} \sim 23$ K).

III. RESULTS AND DISCUSSION

To determine the crystal structure, we acquired synchrotron x-ray and neutron-diffraction pattern at several temperatures. In general, most of the cubic spinels adopt the $Fd\bar{3}m$ space group. In $LiFeCr_4O_8$, the presence of a (200) superlattice peak in synchrotron x-ray and neutron-diffraction patterns at 298 K, as marked in Fig. 1(a) and Fig. 2(a), indicates that the symmetry is reduced to $F\bar{4}3m$. It should be noted that the (200) peak is forbidden in the $Fd\bar{3}m$ space group. Rietveld analysis of the room-temperature synchrotron [Fig. 1(a)] and neutron pattern [Fig. 2(a)] confirms that the title compound has a noncentrosymmetric $F\bar{4}3m$ space group, as reported for $LiMCr_4O_8$ (M = Ga and In) [26,27], which results from chemical ordering of Li^+ and Fe^{3+} ions at the A site. We did not observe any significant inversion or Li^+/Fe^{3+} antisite disorder in the Rietveld refinement of neutron pattern. The structural parameters obtained from the refinement of neutron pattern at 298 K are given in Table I. The structure remains $F\bar{4}3m$ down to 30 K, as evident from the Rietveld analysis of synchrotron x-ray diffraction (XRD) pattern at 30 K [Fig. 1(b)] and neutron pattern (Fig. S1 in the Supplemental Material [32]), where the (400) reflection remains a single peak [see inset of Figs. 1(a) and 1(b)]. Unlike $LiMCr_4O_8$ (M = Ga, In), this compound undergoes a complete structural transformation to a tetragonal structure ($I\bar{4}m2$) at low temperatures, as revealed by the

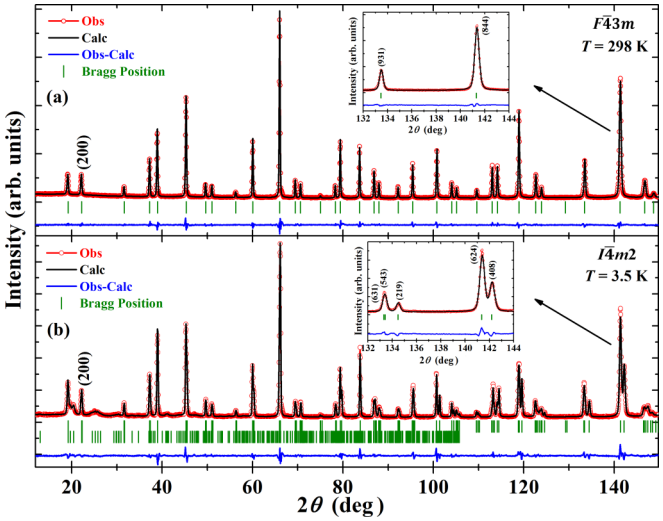

FIG. 2. Rietveld refinements on the neutron-diffraction pattern of $LiFeCr_4O_8$ collected at (a) 298 K and (b) 3.5 K with $\lambda = 1.6$ Å. The first and second Bragg positions in (b) correspond to nuclear and magnetic reflections, respectively.

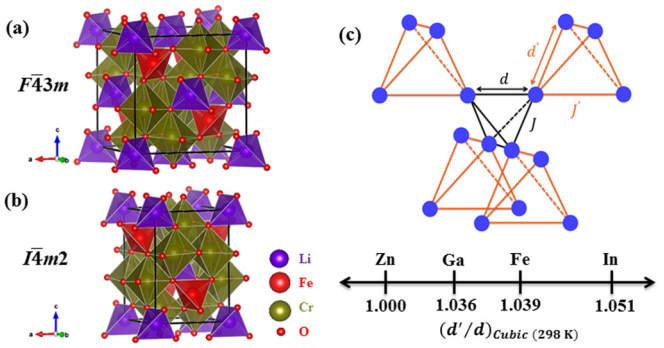

FIG. 3. Schematic representation of the (a) cubic ($F\bar{4}3m$) and (b) tetragonal ($I\bar{4}m2$) structure of $LiFeCr_4O_8$ at 298 K and 3.5 K, respectively, obtained from the Rietveld refinements on the neutron-diffraction data. (c) Schematics of the breathing pyrochlore lattice where the distortion (d'/d) on the Cr_4 network varies with the ionic radii of the A-site ion. The distortion for the Ga and In compound has been calculated based on the Cr-Cr bond distances reported in Ref. [35].

Rietveld refinement of synchrotron [Fig. 1(c)] and neutron [Fig. 2(b)] pattern at 20 and 3.5 K, respectively. The splitting of the (400) peak into the (220) and (004) peaks due to the tetragonal transition is shown in the inset of Fig. 1(c). Additional synchrotron pattern are given in the Supplemental Material (Fig. S2) [32]. Considering the low-temperature magnetic transition at 23 K, as discussed later in Sec. III, it is conceivable that the structural transition is coupled to this magnetic transition and occurs at the same temperature. It should be noted that such a magnetostructural transition occurs in the A-site ordered $LiMCr_4O_8$ (M = Ga and In) [26,27] and ACr_2O_4, (A = Zn, Cd, Hg) due to dominant frustration in the pyrochlore lattice [13–15]. This suggests that the magnetic frustration is dominant at low temperatures in the present system as well. The low-temperature neutron pattern [Fig. 2(b)] also include magnetic structure refinement, which will be discussed later. The structural parameters obtained from the refinement of the neutron data at 298 K and 3.5 K are given in Tables I and II, respectively.

Figures 3(a) and 3(b) show a schematic of both cubic and tetragonal crystal structures, respectively. In the cubic structure, Li and Fe are present in the 4a and 4d Wyckoff positions, respectively, while Cr and O both occupy different 16e Wyckoff sites. In the tetragonal structure, Li and Fe are present at 2a and 2d Wyckoff positions, respectively, while Cr and O occupy different 8i Wyckoff sites similar to that found in MgV_2O_4 [33] and other A-site ordered compounds [34]. The ordering of A-site ions becomes favorable due to the difference in their valence states in the equivalent crystallographic sites leading to the minimization of electrostatic energy. The zinc-blende type of ordering between Li^+ and Fe^{3+} ions at the A-site of chromate spinel results in a different amount of chemical pressure on the pyrochlore network (Cr_4) leading to the modulation of Cr-Cr bond lengths, as seen in Fig. 3(c). There are two different Cr-Cr distances, 2.983 Å and 2.870 Å, in the cubic structure, which are associated with large

TABLE I. Structural parameters of $LiFeCr_4O_8$ obtained from the Rietveld refinement of neutron diffraction data acquired at 298 K.

$LiFeCr_4O_8$ (Space group: $F\bar{4}3m$)
$a = 8.27779\,(1)$ Å

Atom	x	y	z	B_{iso} (Å^2)	Occupancy
Li (4a)	0	0	0	0.84 (12)	1.0
Fe (4d)	0.75	0.75	0.75	0.41 (2)	1.0
Cr (16e)	0.3726 (3)	0.3726 (3)	0.3726 (3)	0.22 (2)	1.0
O1 (16e)	0.1372 (1)	0.1372 (1)	0.1372 (1)	0.30 (3)	1.0
O2 (16e)	0.6171 (1)	0.6171 (1)	0.6171 (1)	0.46 (2)	1.0

$R_B = 2.18\%$; $R_F = 1.75\%$; $\chi^2 = 5.32\%$

Bonds	Distance (Å)
4 × (Li-O1)	1.9668 (10)
4 × (Fe-O2)	1.9050 (9)
3 × (Cr-O1)	1.9521 (27)
3 × (Cr-O2)	2.0277 (26)

TABLE II. Structural parameters of $LiFeCr_4O_8$ obtained from the Rietveld refinement of neutron diffraction data acquired at 3.5 K.

$LiFeCr_4O_8$ (Space group: $I\bar{4}m2$)
$a = 5.85755(1)$ Å, $c = 8.24301\,(3)$ Å

Atom	x	y	z	B_{iso} (Å^2)	Occupancy
Li ($2a$)	0	0	0	1.07 (19)	1.0
Fe ($2d$)	0.0	0.5	0.75	0.20 (0)	1.0
Cr ($8i$)	0.2546 (7)	0	0.6272 (5)	0.20 (0)	1.0
O1 ($8i$)	0.7661 (3)	0	0.3834 (3)	0.29 (2)	1.0
O2 ($8i$)	0.7249 (3)	0	0.8642 (3)	0.29 (2)	1.0

$R_B = 2.87\%$; $R_F = 1.90\%$; $\chi^2 = 3.47\%$

Bonds	Distance (Å)
2 × (Li-O2)	1.9642 (19)
2 × (Li-O2)	1.9642 (31)
2 × (Fe-O1)	1.9088 (19)
2 × (Fe-O1)	1.9088 (31)
(Cr-O1)	2.0225 (74)
2 × (Cr-O1)	2.0169 (52)
(Cr-O2)	1.9460 (74)
2 × (Cr-O2)	1.9586 (52)

and small Cr_4 tetrahedra, respectively, reflecting the role of A-site cation ordering in $LiFeCr_4O_8$. On the other hand, we observe four inequivalent Cr-Cr distances in the tetragonal structure ($I\bar{4}m2$): 2.895 Å and 2.869 Å (small Cr_4 tetrahedra), and 2.963 Å and 2.973 Å (large Cr_4 tetrahedra). The relative difference between the long and short bonds in the small and large tetrahedra is 0.025 Å and 0.011 Å, respectively. The distortion of the pyrochlore lattice is characterized by the ratio of Cr-Cr distance in the large and small tetrahedra (d'/d), which is inversely related to the breathing factor B_f (J'/J) [26]. We obtain a distortion of 1.039 for the Fe compound, which lies between that of the Ga (1.036) and In (1.051) compound [35].

In Fig. 4(a), we show the temperature-dependent dc magnetization data, $M\,(T)$, measured with an applied magnetic field of 0.1 kOe for zero-field-cooled (ZFC) and field-cooled (FC) conditions. In spinels, the strongest magnetic interaction is between the A- and B-site magnetic ions. Therefore, the highest magnetic transition at 94 K indicates ferrimagnetic ordering due to antiferromagnetic coupling between the Fe^{3+} and Cr^{3+} ions. However, the antiferromagnetic interaction is relatively weak for half-filled Fe^{3+}: t_2 orbital and empty Cr^{3+}: e_g orbital, according to symmetry and electrostatic consideration [4]. Further, only 50% of the tetrahedral sites are occupied by Fe^{3+} ions. Below the ferrimagnetic transition at 94 K, the $M\,(T)$ data exhibit a maximum around 60 K and sharp fall at 23 K. The origin of magnetic anomaly at 60 K could be related to the spin-gap state (T_{SG}) arising from the modulation of Cr-Cr distances as found in $LiInCr_4O_8$ [34]. The magnetic transition at 23 K is coupled to a first-order structural phase transition, as discussed before. In the temperature-dependent C_p/T data, we also observe anomalies at three transition temperatures, i.e., 94, 60, and 23 K [Fig. 4(b)], which further confirms the aforementioned magnetic phase transitions. Below the magnetostructural transition, we see a small divergence between ZFC and FC magnetization data in the presence of a magnetic field of 0.1 kOe. With increasing magnetic field, the divergence initially increases and then decreases. In the upper inset of Fig. 4(a), we show the dM/dT vs temperature at various magnetic fields showing two magnetic phase transitions at 23 and 94 K, which are also dependent on the applied magnetic field. On applying a magnetic field of 70 kOe, the anomaly at 23 K is suppressed.

From the Curie-Weiss fitting ($\chi = C/T - \theta$) of the temperature-dependent susceptibility data at 0.1 kOe in the temperature range of 250–390 K (Fig. 5), we obtain an effective magnetic moment (μ_{eff}) of 10.69 μ_B/f.u., which is slightly higher than the theoretical value of 9.74 μ_B/f.u. The obtained value of paramagnetic intercept, $\theta_{CW} = -1156$ K, indicates that the average magnetic interaction is strongly antiferromagnetic in nature with the frustration index, $f = |\theta_{CW}|/T_N = 12$. This value is less than those of the corresponding A-site ordered Ga (42) and In (26) compounds. The significant frustration index of the Fe compound indicates that even in the magnetically ordered state, the geometrical frustration exists among Cr ions and this frustration is the driving force for the change in magnetic structure from the metrically cubic ferrimagnetic to the complex spin structure along with concomitant tetragonal structural transition at 23 K. In addition, we suggest that the existence of frustration below magnetic ordering could be an important criterion to have a spin-gap state at 60 K. To confirm the existence of a spin-gap state at 60 K, we need to carry out an inelastic neutron-scattering experiment across the onset of the spin-gap transition. The fact that the distortion parameter (d'/d) of Fe is between that of the Ga and In compounds and the weak interaction between the Fe^{3+} and Cr^{3+} ions qualitatively supports the existence of a gapped state in the Fe compound. Isothermal magnetization data recorded as a function of magnetic field at different temperatures are shown in the bottom inset of Fig. 4(a), where we see clear magnetic hysteresis at all temperatures below ferrimagnetic

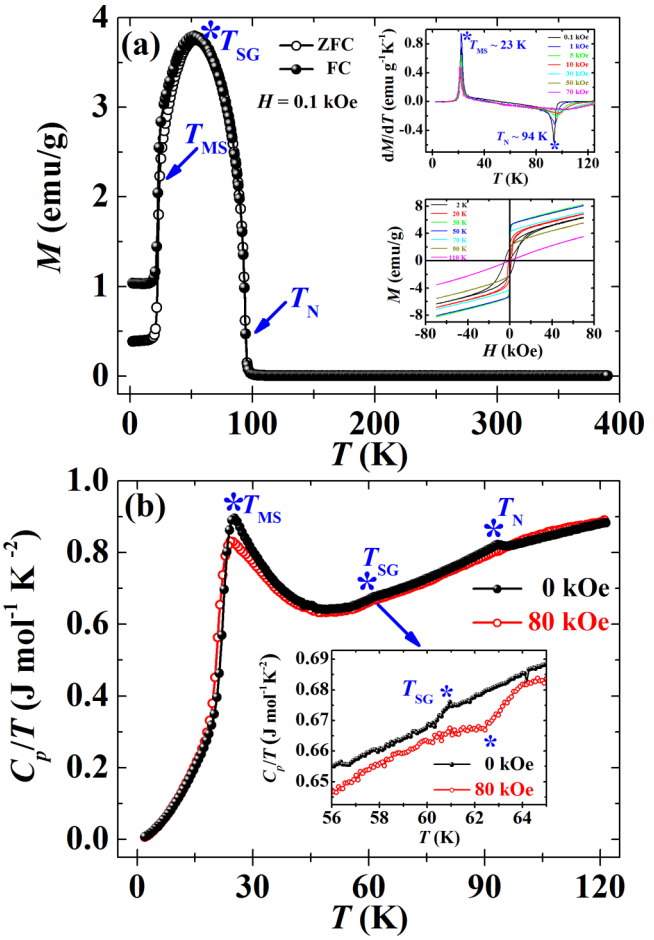

FIG. 4. (a) Temperature dependence of dc magnetization, $M(T)$, of $LiFeCr_4O_8$ at 0.1 kOe. The upper inset of (a) shows the first-order derivative of magnetization with respect to temperature plotted against temperature, and the bottom inset of (a) shows the isothermal magnetization data, $M(H)$, as a function of magnetic field at different temperatures. (b) Temperature dependence of specific heat divided by temperature (C_p/T) for $LiFeCr_4O_8$. T_{MS}, T_{SG}, and T_N stands for magnetostructural, spin-gap, and Néel transition temperatures, respectively.

ordering. It is important to note that above 20 K, the coercive field of the loop decreases as compared to the low-temperature hysteresis, which is consistent with the fact that the magnetic structures are different below and above 23 K.

We have investigated the magnetic structures of $LiFeCr_4O_8$ by performing the Rietveld analysis on the neutron powder pattern collected at low temperatures. In the temperature range $30 \leqslant T \leqslant 94$ K, we do not observe any new reflection other than an increase in intensity on top of some nuclear reflection and therefore we considered the propagation vector, $\mathbf{k} = (0,0,0)$, for the cubic phase. We have found that the refinement of the magnetic structure by considering the three-dimensional (3D) representation Γ_4, as provided by BasIreps, gives the best fit to the observed diffraction patterns at $30 \leqslant T \leqslant 94$ K. The true direction of the magnetic moment cannot be determined with powder diffraction in a cubic lattice; however, considering the highest possible magnetic symmetry, we should assume that the magnetic moment direction of both Fe^{3+} and Cr^{3+} ions is mostly along the c axis of one of the maximal subgroups of

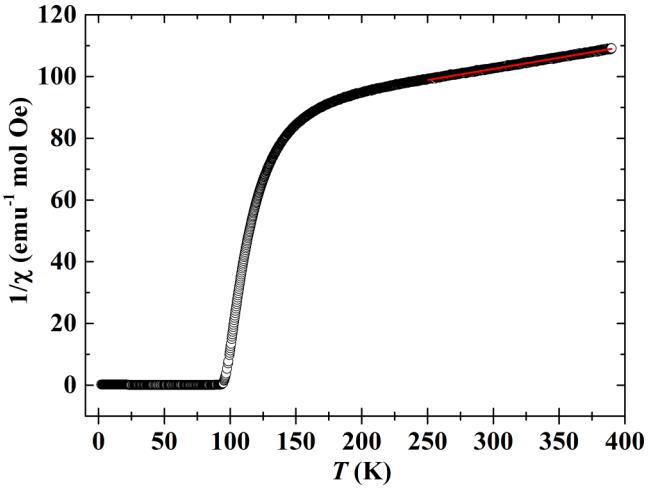

FIG. 5. Temperature dependence of inverse susceptibility of $LiFeCr_4O_8$ at 0.1 kOe. The linear fitting of the inverse susceptibility data in the temperature range of 250–390 K is shown in red.

the paramagnetic group $F\bar{4}3m1'$, the Shubnikov group $I\bar{4}m'2'$ as determined with k-SUBGROUPSMAG [36]. The tetragonal distortion is too weak to be observed in this temperature range and the lattice remains metrically cubic. With this symmetry, the orientation of the magnetic moment of Fe^{3+} ions is strictly along c, but Cr^{3+} moments can have the following components: $\mathbf{m} = (m_x, m_x, m_z)$. However, the refined m_x component is zero within the standard deviation, so in the final refinement it was fixed to zero. The fitted pattern at 30 K is shown in Fig. 6(a) and the corresponding magnetic structure is collinear ferrimagnetic (Fe^{3+} and Cr^{3+} ions are aligned antiparallel) in nature [Fig. 6(b)]. The magnitude of the magnetic moments of Fe^{3+} and Cr^{3+} ions at 30 K is 2.54(16) μ_B and 0.28(11) μ_B, respectively.

We have determined the magnetic structure associated with the tetragonal phase ($I\bar{4}m2$) which appears below 23 K. Preliminary modeling on the neutron powder pattern collected at 3.5 K showed the presence of two different propagation vectors, $\mathbf{k}_1 = (0,0,0)$ and the inconmensurate $\mathbf{k}_2 = (1/2,\delta,1/2)$ with $\delta = 0.4383(4)$. This is the Q point of the Brillouin zone of $I\bar{4}m2$. The first propagation vector

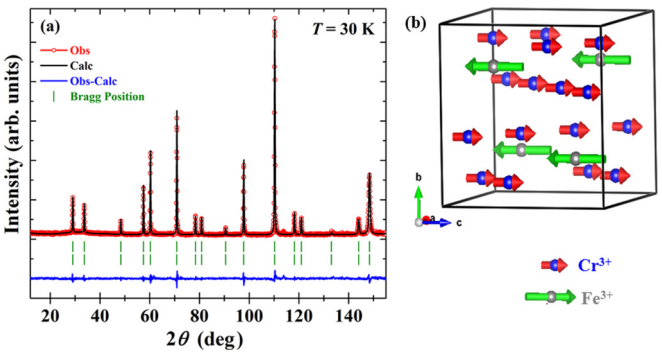

FIG. 6. (a) Rietveld refinement on the neutron-diffraction pattern of $LiFeCr_4O_8$ collected at $T = 30$ K ($\lambda = 2.4$ Å) and (b) the corresponding schematic of collinear ferrimagnetic structure of the compound obtained from the refinement.

is related with the ferrimagnetic component already present below 94 K and the second propagation vector is related to a strong magnetoelastic coupling giving rise to a clearly visible structural distortion approximately described by the space group $I\bar{4}m2$. The extended little group is, in fact, monoclinic $G_{k,-k} = I1m1 = Im$ and the corresponding maximal magnetic superspace group is $Im1'(1/2,\delta,1/2)0s$ [the standard superspace group symbol as provided by ISODISTORT [37] is $Bm1'(0,1/2,g)0s$ following a basis change with respect to the parent group $I\bar{4}m2$]. The symmetry constraints for this magnetic superspace group give rise to 21 free parameters so that additional constraints are needed to treat the powder pattern. The presence of the propagation vector $\mathbf{k_1} = (0,0,0)$ breaks the symmetry so that the operation $\{1'|0,0,0,1/2\}$ is not allowed, reducing the symmetry to Im (1/2, δ, 1/2)0. To treat the data, we have decided to use a simpler approach, implemented in the program FULLPROF [31], for treating conical structures often found in spinel structures [38].

The expression of the magnetic interaction vector (perpendicular component of the magnetic structure factor to the scattering vector **h**) of fundamental reflections $\mathbf{h} = \mathbf{H}$ (**H** is a reciprocal lattice vector of the crystal structure) is given by

$$|\mathbf{M}_\perp(\mathbf{H})|^2 = (p \sin\omega)^2 \left[\sum_{j=1}^{n} m_j f_j(h) \cos\beta_j \exp(2\pi i \mathbf{H}\mathbf{r}_j)\right]^2.$$

For satellite magnetic reflections $\mathbf{h} = \mathbf{H} + \mathbf{k}$, the expression is

$$|\mathbf{M}_\perp(\mathbf{H} \pm \mathbf{k})|^2 = p^2 \left(\frac{1+\cos^2\omega}{4}\right) \times \left[\sum_{j=1}^{n} m_j f_j(h) \sin\beta_j \exp(2\pi i \mathbf{H}\mathbf{r} \mp \varphi_j)\right]^2.$$

The coefficient $p = 0.26954$ is the conversion of Bohr magnetons to scattering length, ω is the angle between the cone axis and the scattering vector **h**. m_j, $f_j(h)$, β_j, and φ_j are, respectively, the magnitude of the magnetic moment, the magnetic form factor, the cone angle, and the phase for the atom j.

In our case, for one Fe atom and four Cr atoms in the primitive cell, the total number of free parameters we have used is eight: magnetic moment of Fe^{3+}, common magnetic moment of all Cr^{3+} ions, cone angle of Fe^{3+} moments, common cone angle of Cr^{3+} moments (attempts to refine them independently give rise to instabilities or to negligible departures with respect to the common cone angle hypothesis), and the four phases of Cr^{3+} atoms (the phase of Fe is fixed to zero). The orientation of the cone axis contains two more parameters, but we have restricted this by fixing this axis along the *b* axis. With this model and taking into account the broadening of the $\mathbf{H} + \mathbf{k}_2$ magnetic reflections, we have refined the crystal and magnetic structure, combining the data from two different wavelengths of D2B. The broadening of the magnetic reflections has been taken into account considering that the correlation length follows a platelet-type shape perpendicular to the incommensurate direction of the propagation vector. The shortest correlation length is only of ≈62 Å along **b** (≈0 unit cells). The magnetic parameters obtained from the refinement of neutron data at 3.5 K are given in the Supplemental Material (Table S1) [32]. A schematic view of the magnetic structure at 3.5 K is shown in Fig. 7.

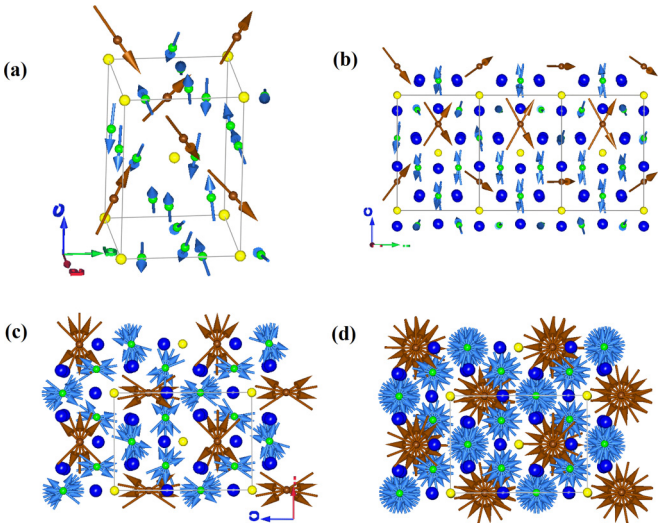

FIG. 7. Magnetic structure of $LiFeCr_4O_8$ obtained from the Rietveld refinement on the neutron-diffraction pattern collected at 3.5 K. View of the magnetic structure: (a) in an arbitrary orientation to show the strongly noncollinear character; (b) along the *a* axis (3 unit cells along *b* show the ferrimagnetic component); (c),(d) along the *b* axis with 4.5 and 11 unit cells show the helical part of the spin configuration. The brown and green solid circles indicates Fe and Cr atoms, respectively.

Now we discuss the dielectric properties of $LiFeCr_4O_8$. The temperature-dependent dielectric data show three anomalies at 94 K, 60 K, and 23 K, as shown in Fig. 8(a). The dielectric anomaly at 94 K is associated with the ferrimagnetic ordering. The occurrence of dielectric anomaly at 23 K is consistent with magnetostructural coupling. The evolution of dielectric anomalies at the three magnetic transition temperatures indicates the coupling between magnetization and dielectric response. It should be emphasized here that a dielectric anomaly at the spin-gap transition is seldom reported in the literature. The temperature dependence of the dielectric anomalies is found to be very robust with different measuring frequencies. To understand the response of the dielectric constant to an external magnetic field, we carried out a temperature-dependent dielectric constant measurement in the presence of applied magnetic fields, as shown in Fig. 8(b), and the corresponding temperature-dependent dielectric loss in the inset of Fig. 8(b). The dielectric anomalies at T_N and T_{SG} are suppressed by the applied magnetic fields. Moreover, we observe a small shift of the dielectric peak at $T_{SG} \sim 60$ K to higher temperatures with increasing magnetic field. In the absence of ferroelectricity, the origin of magnetodielectric coupling has been attributed to spin-lattice coupling as revealed by our Raman results, as discussed later. The temperature-dependent dielectric loss in the presence of different magnetic fields also shows a suppressed feature as well as a shift of the loss peak to higher temperatures with increasing magnetic field [inset of Fig. 8(b)]. It may be mentioned here that though the magnetic space group $I\bar{4}m'2'$ allows a magnetoelectric effect in the ferrimagnetic phase [23], we did not observe any indication for the presence of a magnetoelectric effect up to a magnetic field

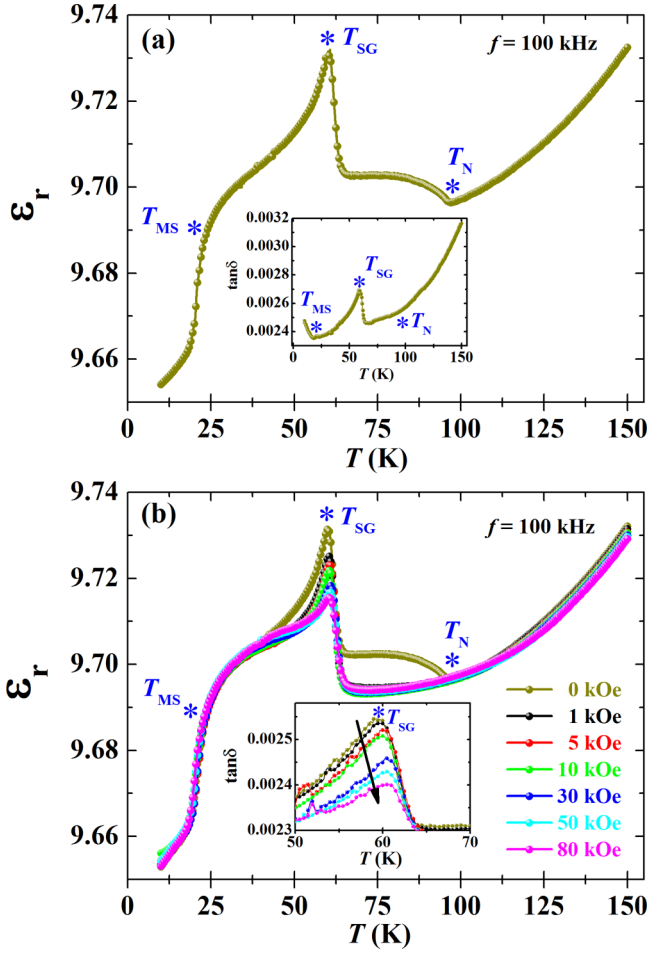

FIG. 8. (a) Temperature dependence of the dielectric constant of $LiFeCr_4O_8$ in zero magnetic field at 100 kHz. The inset of (a) shows the temperature dependence of the dielectric loss in zero magnetic fields at 100 kHz. (b) Temperature dependence of the dielectric constant in the presence of different magnetic fields at 100 kHz. The inset of (b) shows the temperature-dependent dielectric loss in the presence of different magnetic fields at 100 kHz.

of 9 T after magnetoelectric poling with an external electric field of 9.7 kV/cm in the presence of different magnetic fields.

To further explore the effect of magnetic field on the temperature-dependent dielectric constant, we have investigated the isothermal magnetocapacitance (% MC) as a function of magnetic field, as shown in Figs. 9(a)–9(f). From this figure, we see that there is a magnetodielectric hysteresis with magnetic field at all temperatures below ferrimagnetic transition. Since there exists an isothermal magnetic hysteresis below the ferrimagnetic ordering temperature as a function of magnetic field [Figs. 9(g)–9(l)], the hysteretic behavior of the magnetocapacitance (%MC) could be directly correlated with the magnetization data. Interestingly, we notice that the width of the magnetodielectric hysteresis also changes with changing temperature similar to that observed in the magnetic hysteresis, indicating that spin-spin interactions are the driving force for the magnetodielectric effect. More surprisingly, we see from Figs. 9(a) and 9(b) that there is a reversal in direction of the magnetodielectric hysteresis as compared to the magnetocapacitance data above the magnetostructural

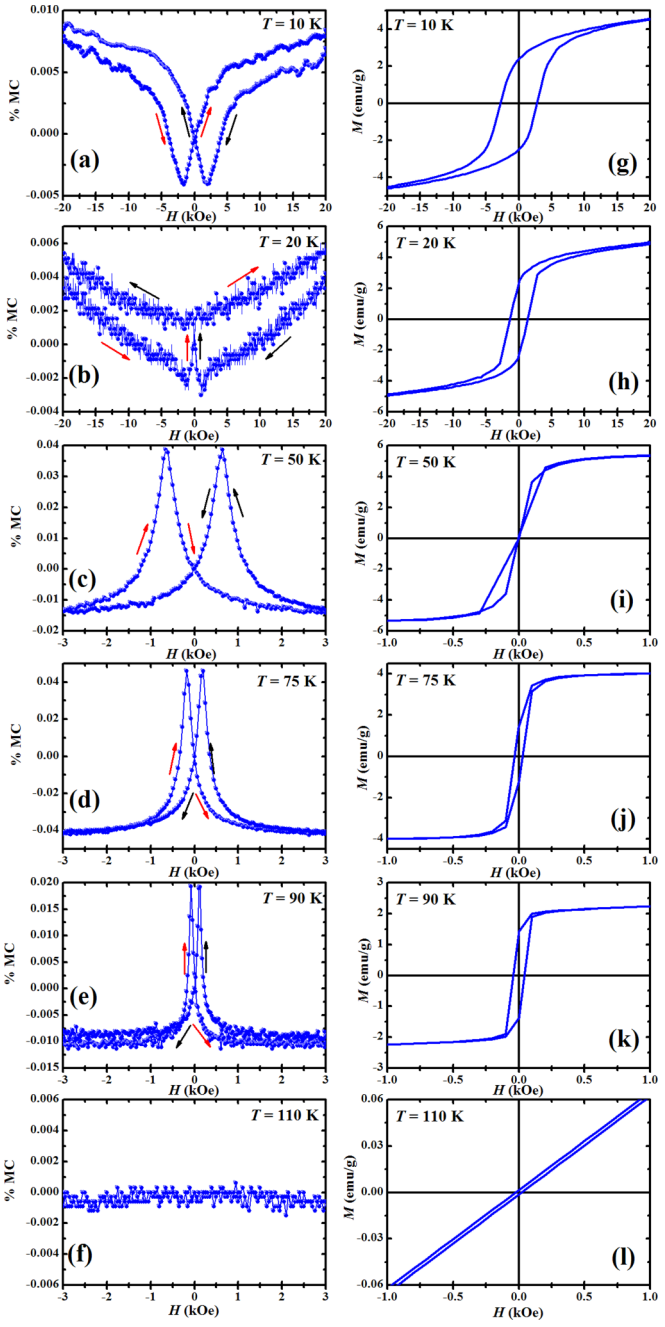

FIG. 9. (a)–(f) Magnetocapacitance (% MC) hysteresis and (g)–(i) isothermal magnetization hysteresis of $LiFeCr_4O_8$ as a function of magnetic field at different temperatures.

phase transition temperature. We attribute the reversal of the magnetodielectric hysteresis to the change in magnetic and crystal structures below 23 K. The increased width of magnetodielectric hysteresis near the spin-gap state [Fig. 6(c)] is noteworthy and it could be associated with the increased cation off-centering as a result of stronger breathing distortion facilitating to form the gapped state [39].

Raman measurements have been carried out on $LiFeCr_4O_8$ at 290 K and in the temperature range of 5–130 K. The Raman spectrum of $LiFeCr_4O_8$ acquired at 290 K is shown in Fig. 10(a). $LiFeCr_4O_8$, which consists of Raman signatures of LiO_4, FeO_4 tetrahedra, and CrO_6 octahedra, very similar to

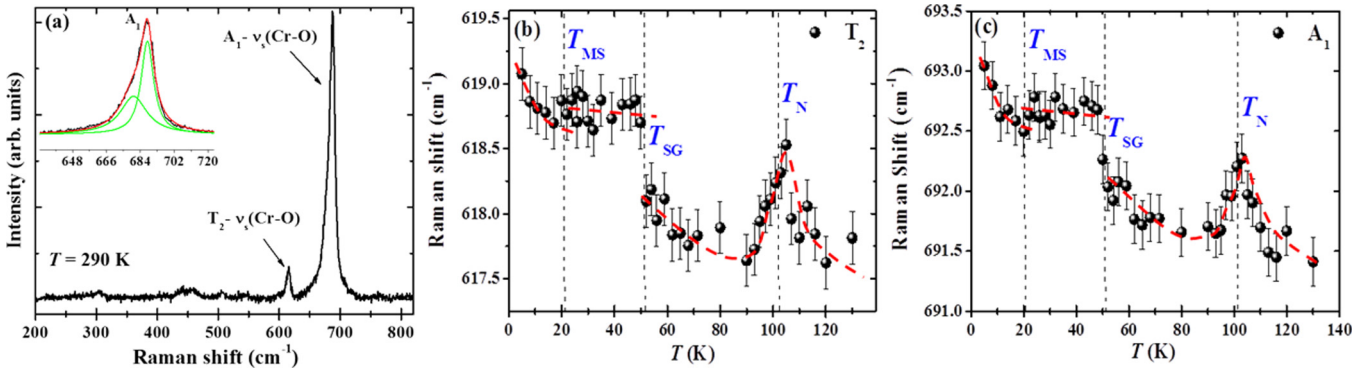

FIG. 10. (a) Raman spectra of $LiFeCr_4O_8$ at 290 K. The inset shows the deconvolution of the Cr-O stretching mode (A_1); (b),(c) Temperature dependence of the T_2 (left panel) and A_1 (right panel) modes. The dashed lines correspond to the transition temperatures and the red lines are a guide to the eyes.

that of normal spinels. Compared to the Raman spectrum of a cubic ($Fd\bar{3}m$) spinel structure, a few modes in $LiFeCr_4O_8$ have been found to be split into two. For example, the A_1 mode (which corresponds to symmetric Cr-O stretching in the CrO_6 octahedra) in the conventional spinel, e.g., $ZnCr_2O_4$, is a singlet which split into two peaks at 689 and 692 cm^{-1} in $LiFeCr_4O_8$ [40]. This is due to lifting of the degeneracy of the modes arising due to the presence of different Cr-O bond lengths within CrO_6 octahedra, as discussed before. There is a prominent Raman peak that occurs at ~618 cm^{-1} (T_2). Both A_1 and T_2 modes can be attributed to the symmetric stretching of the Cr-O bonds in the CrO_6 octahedra [40]. The temperature dependence of these two modes (692 and 618 cm^{-1}) is shown in Figs. 10(b) and 10(c), respectively. As a general rule, the frequencies of the Raman modes increase with decreasing temperature, with contributions from the anharmonicity in the lattice contraction, which is the case with both A_1 and T_2 modes above T_N. In accordance with magnetization, heat capacity, and dielectric anomalies, the temperature dependence of the frequency of these modes deviates from the anharmonic behavior and exhibits anomalous behavior at T_{MS}, T_{SG}, and T_N. Upon lowering the temperature, both modes exhibit a maximum in the vicinity of T_N. This is because of the development of antiferromagnetic coupling between the A-site Fe^{3+} and B-site Cr^{3+} ions as it approaches the Néel transition, causing a compressive stress on the CrO_6 octahedra which results in hardening of these modes immediately above T_N. Upon achieving the ferrimagnetic ordering, the stress is relaxed, leading to a decrease of phonon-mode frequencies. Above the ferrimagnetic transition, these modes follow the expected anharmonic behavior upon decreasing the temperature. It is interesting to note that the full width at half maxima (FWHM), which is associated with the lifetime of the phonons during such transitions, shows no anomaly, giving a clear indication that there is no interaction between spin and phonon energies. Similar to the dielectric anomaly around T_{SG}, we see an abrupt increase in frequency of both of the phonon modes. This is again due to the opening of a spin-gap state which constricts the CrO_6 octahedra, leading to a resulting strain. Since there is a competition between the A-B site ordering and B-site ordering, the strain is released only at the magnetostructural transition at 23 K, below which we observe the hardening of the phonon modes. We would like to mention here that the competing strains mentioned above could be the reason for the magnetostructural transition observed at 23 K. In contrast to the frequency shifts, the line widths of these modes do not show any noticeable change within the resolution of our experiment across these transitions. Therefore, we suggest a role for spin-lattice coupling as the underlying mechanism responsible for coupling between magnetism and dielectric properties in this unique A-site cation-ordered compound.

IV. CONCLUSIONS

We have demonstrated that the A-site cation-ordered spinel $LiFeCr_4O_8$ is a unique system which holds breathing distortion of a frustrated pyrochlore Cr lattice and antiferromagnetic coupling between Fe^{3+} and Cr^{3+} ions. Consequently, the compound exhibits a magnetostructural transition ($T_N \sim$ 23 K), spin-gap ($T_{SG} \sim$ 60 K), and ferrimagnetic ordering at $T_N \sim$ 94 K. Interestingly, dielectric anomalies are observed at all three magnetic transitions, indicating magnetodielectric effects. The origin of magnetodielectric effects has been attributed to the spin-lattice coupling as evidenced from Raman spectroscopic measurements. The occurrence of magnetostructural coupling reveals that the magnetic frustration dominates over antiferromagnetic coupling between Fe^{3+} and Cr^{3+} ions, which makes this system further interesting.

ACKNOWLEDGMENTS

A.S. would like to acknowledge the financial support from the Science and Engineering Board (SERB Sanction No. EMR/2014/000896), Department of Science & Technology (DST), Government of India and Sheikh Saqr Laboratory (SSL) at Jawaharlal Nehru Centre for Advanced Scientific Research (JNCASR). R.S. and A.S. would like to acknowledge (DST) for providing the financial support to perform neutron-diffraction experiments at the Institut Laue Langevin, Grenoble, France and also for facilitating the synchrotron x-ray diffraction experiments at the Indian Beamline, Photon Factory, KEK, Japan. R.S. would like to thank JNCASR for providing financial support through a Ph.D. scholarship (JNC/S0154) and SSL for financial support through the research associate fellowship (JNC/SSL/CNR/6001). C.N. would like to thank the SSL for financial support through the RAKCAM Senior Fellow program.

[1] J. B. Goodenough, in *Magnetism and the Chemical Bond*, edited by F. A. Cotton (Interscience Publishers, New York, 1963).
[2] B. Canals and C. Lacroix, Phys. Rev. B **61**, 1149 (2000).
[3] A. Ramirez, Annu. Rev. Mater. Sci. **24**, 453 (1994).
[4] D. Wickham and J. B. Goodenough, Phys. Rev. **115**, 1156 (1959).
[5] J. B. Goodenough, Phys. Rev. **117**, 1442 (1960).
[6] E. Verwey, Nature (London) **144**, 327 (1939).
[7] M. S. Senn, J. P. Wright, and J. P. Attfield, Nature (London) **481**, 173 (2012).
[8] N. Tristan, J. Hemberger, A. Krimmel, H.-A. Krug von Nidda, V. Tsurkan, and A. Loidl, Phys. Rev. B **72**, 174404 (2005).
[9] W. Roth, J. Phys. **25**, 507 (1964).
[10] W. Roth, J. Phys. Chem. Solids **25**, 1 (1964).
[11] B. Boucher, A. Herpin, and A. Oles, J. Appl. Phys. **37**, 960 (1966).
[12] H. S. Nair, Z. Fu, J. Voigt, Y. Su, and T. Brückel, Phys. Rev. B **89**, 174431 (2014).
[13] S.-H. Lee, C. Broholm, W. Ratcliff, G. Gasparovic, Q. Huang, T. Kim, and S.-W. Cheong, Nature (London) **418**, 856 (2002).
[14] M. Matsuda, M. Takeda, M. Nakamura, K. Kakurai, A. Oosawa, E. Lelièvre-Berna, J.-H. Chung, H. Ueda, H. Takagi, and S.-H. Lee, Phys. Rev. B **75**, 104415 (2007).
[15] H. Ueda, H. Mitamura, T. Goto, and Y. Ueda, Phys. Rev. B **73**, 094415 (2006).
[16] V. Kocsis, S. Bordács, D. Varjas, K. Penc, A. Abouelsayed, C. A. Kuntscher, K. Ohgushi, Y. Tokura, and I. Kézsmárki, Phys. Rev. B **87**, 064416 (2013).
[17] Y. Yamashita and K. Ueda, Phys. Rev. Lett. **85**, 4960 (2000).
[18] O. Tchernyshyov, R. Moessner, and S. L. Sondhi, Phys. Rev. Lett. **88**, 067203 (2002).
[19] S. Bordács, D. Varjas, I. Kézsmárki, G. Mihály, L. Baldassarre, A. Abouelsayed, C. A. Kuntscher, K. Ohgushi, and Y. Tokura, Phys. Rev. Lett. **103**, 077205 (2009).
[20] L. I. Vergara, J. Cao, N. Rogado, Y. Q. Wang, R. P. Chaudhury, R. J. Cava, B. Lorenz, and J. L. Musfeldt, Phys. Rev. B **80**, 052303 (2009).
[21] S. Lee, A. Pirogov, M. Kang, K-H. Jang, M. Yonemura, T. Kamiyama, S.-W. Cheong, F. Gozzo, N. Shin, H. Kimura, Y. Noda, and J.-G. Park, Nature (London) **451**, 805 (2008).
[22] R. Saha, S. Ghara, E. Suard, D. H. Jang, K. H. Kim, N. V. Ter-Oganessian, and A. Sundaresan, Phys. Rev. B **94**, 014428 (2016).
[23] S. Ghara, N. V. Ter-Oganessian, and A. Sundaresan, Phys. Rev. B **95**, 094404 (2017).
[24] B. Roy, A. Pandey, Q. Zhang, T. W. Heitmann, D. Vaknin, D. C. Johnston, and Y. Furukawa, Phys. Rev. B **88**, 174415 (2013).
[25] V. P. Sakhnenko and N. V. Ter-Oganessian, J. Phys.: Condens. Matter **24**, 266002 (2012).
[26] N. V. Ter-Oganessian, J. Magn. Magn. Mater. **364**, 47 (2014).
[27] R. Saha, F. Fauth, M. Avdeev, P. Kayser, B. J. Kennedy, and A. Sundaresan, Phys. Rev. B **94**, 064420 (2016).
[28] S. Lee, S.-H. Do, W.-J. Lee, Y. S. Choi, M. Lee, E. S. Choi, A. P. Reyes, P. L. Kuhns, A. Ozarowski, and K.-Y. Choi, Phys. Rev. B **93**, 174402 (2016).
[29] J. Preudhomme and P. Tarte, Spectrochim. Acta Part A: Molec. Spectrosc. **27**, 1817 (1971).
[30] P. Tarte, Spectrochim. Acta **21**, 313 (1965).
[31] J. Rodríguez-Carvajal, Phys. B: Condens. Matter **192**, 55 (1993). The programs of the FULLPROF Suite can be found at https://www.ill.eu/sites/fullprof/.
[32] See Supplemental Material at http://link.aps.org/supplemental/10.1103/PhysRevB.96.214439 for additional neutron-diffraction and synchrotron x-ray diffraction data at different temperatures. It also includes magnetic parameters of the conical spin structure at 3.5 K.
[33] E. M. Wheeler, B. Lake, A. T. M. Nazmul Islam, M. Reehuis, P. Steffens, T. Guidi, and A. H. Hill, Phys. Rev. B **82**, 140406(R) (2010).
[34] G. J. Nilsen, Y. Okamoto, T. Masuda, J. Rodriguez-Carvajal, H. Mutka, T. Hansen, and Z. Hiroi, Phys. Rev. B **91**, 174435 (2015).
[35] Y. Okamoto, G. J. Nilsen, J. P. Attfield, and Z. Hiroi, Phys. Rev. Lett. **110**, 097203 (2013).
[36] J. Perez-Mato, S. Gallego, E. Tasci, L. Elcoro, G. de la Flor, and M. Aroyo, Annu. Rev. Mater. Res. **45**, 217 (2015).
[37] B. J. Campbell, H. T. Stokes, D. E. Tanner, and D. M. Hatch, J. Appl. Crystallogr. **39**, 607 (2006).
[38] D. Lyons, T. Kaplan, K. Dwight, and N. Menyuk, Phys. Rev. **126**, 540 (1962).
[39] T. D. Sparks, M. C. Kemei, P. T. Barton, R. Seshadri, E.-D. Mun, and V. S. Zapf, Phys. Rev. B **89**, 024405 (2014).
[40] Z. M. Stanojević, N. Romčević, and B. Stojanović, J. Eur. Ceram. Soc. **27**, 903 (2007).